

Shattering and Particle Interarrival Times Measured by Optical Array Probes in Ice Clouds

P. R. FIELD, A. J. HEYMSFIELD, AND A. BANSEMER

National Center for Atmospheric Research, Boulder, Colorado

(Manuscript received 11 August 2005, in final form 13 March 2006)

ABSTRACT

Optical array probes are one of the most important tools for determining the microphysical structure of clouds. It has been known for some time that the shattering of ice crystals on the housing of these probes can lead to incorrect measurements of particle size distributions and subsequently derived microphysical properties if the resulting spurious particles are not rejected. In this paper it is shown that the interarrival times of particles measured by these probes can be bimodal—the “cloud” probes are more affected than the “precipitation” probes. The long interarrival time mode represents real cloud structure while the short interarrival time mode results from fragments of shattered ice particles. It is demonstrated for the flights considered here that if the fragmented particles are filtered using an interarrival time threshold of 2×10^{-4} s in three of the four cases and 1×10^{-5} s in the other, then the measured total concentration can be affected by up to a factor of 4 in situations where large particles are present as determined by the mass-weighted mean size exceeding 1 mm, or the exponential slope parameter falling below 30 cm^{-1} . When the size distribution is narrow (mass weighted mean size <1 mm), ice water contents can be overestimated by 20%–30% for the cases presented here.

1. Introduction

The optical array probe (OAP; e.g., Knollenberg 1970, 1981) has been a tool for cloud physics investigations for the past 30 yr. Since the introduction of the OAPs it has been known that artifacts need to be removed from the data before an estimate of the measured size distribution can be obtained. Just over 20 yr ago, two meetings were convened to discuss cloud particle measurements and processing (Baumgardner and Dye 1983; Heymsfield and Baumgardner 1985). One common conclusion from the meetings was that software filters that made use of particle aspect ratio and interarrival time should be used to eliminate the effects of hydrometeor breakup or splashing when colliding with the probe tips. In a Bureau of Reclamation report written following the High Plains Experiment (HIPLEX) project Cooper (1977) wrote that one of the rejection criteria for 2D optical probes used in the analysis of the data was that “If the time interval between images corresponds to a spatial distance of less

than 2.5 cm, the second image is not accepted.” Therefore, while some older processing codes still no doubt contain this particle interarrival time filter, the advent of a new generation of 2D probes and aircraft platforms make it important to characterize this effect and recognize that this rejection criteria will have to be reevaluated for each aircraft and probe combination.

Some recent papers (Field et al. 2003; Korolev and Isaac 2005) have revisited the question of the effect on the measurements of ice particles shattering on the probe housing when traveling at aircraft sampling speeds. These follow from interest in the fidelity of the Forward Scattering Spectrometer Probes (FSSPs) in ice cloud (Gardiner and Hallett 1985; Gayet et al. 1996). Hallett (1976) originally showed that ice particles, 100–200 μm in size, will shatter into dozens of fragments when they collide with a formvar-coated surface at 100 m s^{-1} . It is clear to see that if this occurs on the housing of an OAP and the fragments produced are subsequently sampled then this will lead to an erroneous measurement of the particle size distribution and to possible problems with the determination of microscale spatial structure. Consequently, there is some concern in the experimental and modeling community about the accuracy of microphysical properties and structure

Corresponding author address: Paul Field, NCAR, 3450 Mitchell Lane, Boulder, CO 80301.
E-mail: prfield@ucar.edu

measured by these probes if these fragments are not eliminated.

For the Particle Measuring Systems (PMS) 2D precipitation (2D-P) probe and the Stratton Park Engineering Company (SPEC) High Volume Particle Spectrometer (HVPS), Korolev and Isaac (2005) show a correlation between the maximum particle size observed during a given period and the number of images containing multiple fragments during the same period, interpreted as evidence for breakup of particles either on the probe or in the airflow distortion as it passes or enters the probe. They refrained from interpreting the 2D cloud (2D-C) probe data because the relatively smaller detector width can result in large particles that are largely outside of the sample volume but have protruding arms enter the sample volume, which can give rise to “multiple” particles. The higher resolution and binary nature of the detector also results in some ice particles appearing transparent in places, again generating false multiple particles within a single image frame. However, questions about the breakup of droplets on the inlet of the PMS 260-X, which is physically similar to the 2D-C, have been raised by Jensen and Granek (2002). Although, it should be noted that interarrival time filtering is not possible on the 260-X without major modification to add an interarrival time capability.

In this work we filter out particles that have “zero” interarrival time with the previous particle and make use of area ratio (the ratio of measured pixel area to area covered by a best-fit circle) considerations to filter out image frames that contain multiple images. Here we will look at the interarrival times of the remaining particles and carry out an analysis similar to that presented in Field et al. (2003). In Field et al. it was found that ice particle interarrival times measured with a fast FSSP had two distinct modes and could be modeled well with a mixture of two separate Poisson distributions.

We present an analysis of interarrival time data obtained with the PMS 2D-C, PMS-Droplet Measurement Technologies (DMT) 2D-C-Cloud Imaging Probe (CIP) hybrid, 2D-P, DMT Precipitation Imaging Probe (PIP), and SPEC HVPS probes mounted on a number of different aircraft during flights in ice cloud.

2. Optical array probes

The method of operation of the two-dimensional optical array probe is described in some detail by Knollenberg (1981). Essentially, two-dimensional shadow images of particles are obtained by a linear array of light detectors, housed in one of the probe arms, that rapidly records the shadow caused by particles as they

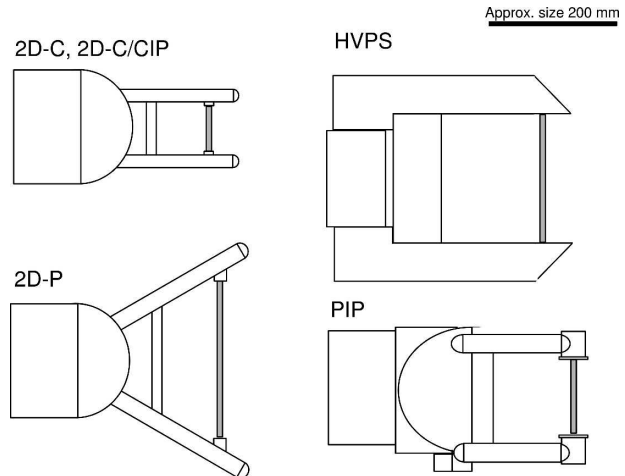


FIG. 1. Schematic diagram of the four optical array probes' inlet housings used in this study. Side view is approximately to scale. Particles enter the probe sample volume from right to left. The probe particle detection lasers are marked in gray (exaggerated width).

occur a laser beam shone from the other probe arm at a rate proportional to the airspeed. Figure 1 is a schematic diagram of the probe housings used to obtain the data presented in this paper. The figure is approximately to scale and shows the side views of the probes as they would be mounted in a PMS canister on an aircraft, with the particles flowing past from right to left. The intention of this figure is to provide the reader with an overview of the different geometries associated with each probe. The PMS 2D-C probe and modified 2D-C probe, with the DMT CIP optoelectronic system replacing the original 2D-C system but not the mechanical structure, has optical arms spaced 61 mm apart that terminate with a hemispherical cap. The optical windows are protected from water streaming along the arms by a raised rim. On other versions of this probe there are “V”-shaped antisplash guards mounted at the top of the rims, but this was not the case for the probes used in this study. The 2D-C and 2D-C-CIP nominally size particles in the range of 25–800 μm , with a pixel size of 25 μm . The temporal resolution of the 2D-C and 2D-C-CIP is 2.5×10^{-7} s. The PMS 2D-P has wider-spaced optical arms (270 mm) to provide an increased sample volume. The optical arms terminate in hemispherical caps and a raised rim protects the optical windows from water streaming along the arms. The 2D-P nominally sizes particles in the size range of 200–6400 μm and has a time resolution of 2.0×10^{-6} s. The SPEC HVPS has a large detector head. The optical arms are spaced 200 mm apart and are terminated by a triangular wedge. The HVPS nominally measures particles in the size range of 200–51 200 μm and has a pixel size of

TABLE 1. Summary of aircraft and particle probes used.

Campaign	Date	Aircraft	True airspeed (m s^{-1})	Cloud probe	Precipitation probe	Location
CRYSTAL-FACE	26 Jul 2002	University of North Dakota (UND) Citation	140	2D-C	HVPS	Under-wing pylon
CAMEX	23 Sep 2001	National Aeronautics and Space Administration DC-8	200	2D-C-CIP	PIP	Under-wing pylon
TRMM	22 Aug 1999	UND Citation	140	2D-C	HVPS	Under-wing pylon
FIRE	26 Nov 1986	National Center for Atmospheric Research King Air	100	2D-C	2D-P	Under-wing pylon

400 μm along the flight direction (for an airspeed of 100 m s^{-1}) and of 200 μm perpendicular to the flight direction. The time resolution of this probe is 4.0×10^{-6} s. The DMT PIP has optical arms spaced 100 mm apart and has the optical windows close to the end of the arms. The optics are protected by a splashguard lip that is flush with the optical windows. The PIP nominally sizes particles in the range of 100–6400 μm and has a time resolution of 10^{-6} s.

3. OAP data processing

Prior to analyzing the interarrival times, the OAP data were passed through the following standard processing.

2D-C, 2D-C-CIP:

- (i) Reject particles with area ratio <0.1 , to remove “streakers” (long, thin images caused by splash or shatter products traveling slower than the true airspeed through the sample volume) and image frames containing multiple particles.
- (ii) Reject particles with area ratio <0.2 and size $<600 \mu\text{m}$, to remove streakers.
- (iii) Reject particles associated with corrupted timelines or timelines indicating all 1 or 0 s.

2D-P, PIP, HVPS:

- (i) Reject particles with area ratio <0.1 , to remove streakers and image frames containing multiple particles.
- (ii) Reject particles associated with corrupted or zero elapsed timelines.

For both “cloud” and “precipitation” probes the depth of field was taken from the probe manuals and the reconstructed technique described in Heymsfield and Parrish (1978) was used to compute sample volume. An additional slice was added to the images (repeat of first slice) to account for the missing slice in the images taken up by the timing information. Elapsed

probe time was calculated as the sum of all particle time bars even if they were rejected (except solid time bars).

Data are presented from four flights: Cirrus Regional Study of Tropical Anvils and Cirrus Layers-Florida Area Cirrus Experiment (CRYSTAL-FACE), Convection and Moisture Experiment (CAMEX), Tropical Rainfall Measuring Mission (TRMM), and First International Satellite Cloud Climatology (ISCCP) Regional Experiment (FIRE). Table 1 gives a summary of the aircraft/probe combinations used.

The CRYSTAL-FACE and TRMM flights were both in thick anvil ice clouds associated with tropical convection with in-cloud temperatures ranging from -12° to -5° and -50° to -15°C , respectively, for the data presented here. In these cases large, irregular particles were present. The majority of the CAMEX flight data covered in-cloud temperatures from -60° to -20°C and was obtained in Hurricane Humberto in 2001. The FIRE flight was in thick, synoptically generated cirrus and aircraft sampling covered in-cloud temperatures ranging from -45° to -25°C .

4. OAP interarrival times

This study focuses on the measured particle interarrival times. Figure 2 shows the interarrival times summed from each particle compared to the buffer elapsed time logged by the data system for a CRYSTAL-FACE flight (26 July 2002). This provides an independent comparison between two separate clock systems. It can be seen that the two elapsed times are consistent to such a degree that the ratio of the two elapsed times has a mean of 1.03 and a standard deviation of 4%. Points where the 2D-C total elapsed time is much lower than the data system buffer time represent periods when the 2D-C probe became overloaded and temporarily shut itself down. The points that have high 2D-C elapsed times (~ 5 s) compared to the data system buffer time are when the buffer included particles with solid time bars. These erroneous buffers were omitted from the analysis.

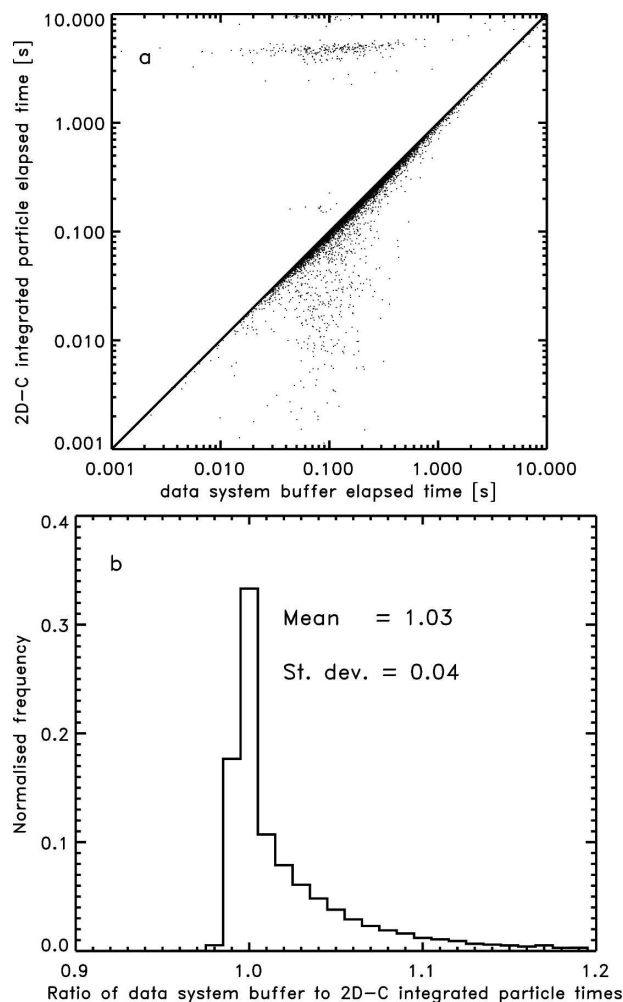


FIG. 2. (a) Scatterplot of elapsed buffer time obtained from the datalogging system clock and by summing the particle interarrival times measured by the 2D-C probe for the CRYSTAL-FACE flight (26 Jul 2002). (b) Histogram of the ratio of the two estimates of buffer elapsed time shown in (a).

Figures 3a,c, 4a,c, 5a,c, and 6a,c show 500 s of interarrival times obtained from the OAPs used during the four flights. These segments of flight data were chosen to try to include some variation over a short time span (in section 5 the reader will be able to assess how representative these sections are when results for the entirety of each flight are presented). Each point represents the interarrival time of a single particle. In Figs. 3a,c, 4a,c, 5a,c, and 6a,c a 20-s period is highlighted with vertical bars for which a histogram of interarrival times is shown in Figs. 3b,d, 4b,d, 5b,d, and 6b,d (logarithmically binned). In the timeframes selected, FIRE and CAMEX display only a single mode of interarrival times, whereas for TRMM and CRYSTAL-FACE a strong bimodal component is seen in the interarrival time data from the 2D-C.

For reference it is noted that for an airspeed of 100 m s^{-1} , interarrival times of 10^{-6} s , 10^{-4} s , and 10^{-2} s are equivalent to mean particle spacings of $100 \text{ } \mu\text{m}$, 10 mm , and 1 m , respectively. By making the simplifying assumption that the OAP sample volumes are defined by the width of the detector array and spacing between the arms we can similarly provide a coarse lower-limit estimate of instantaneous concentrations for interarrival times (given in Table 2).

Figure 3b from the CRYSTAL-FACE flight shows that the short interarrival time mode measured by the 2D-C has a mean around $6 \times 10^{-5} \text{ s}$, while that of the long interarrival time is around 10^{-2} s . It will be seen later that while the mean value of the long interarrival time mode varies considerably (two orders of magnitude), reflecting real cloud structure, the value of the short interarrival time mode is remarkably constant. Figure 3d shows the result from the HVPS, where it can be seen that there is a peak in the number of particles with short interarrival times just above the time resolution of the probe. This is probably just the shoulder of the short interarrival time mode that is evident from the 2D-C but is cutoff by the lower time resolution. The CAMEX data (Fig. 4) show that there is a small mode at short interarrival times for the 2D-C-CIP probe with a mean just below 10^{-6} s . The 2D-C-CIP has the same mechanical structure as in the CRYSTAL-FACE case, but here the probe location, orientation, and airspeed ($\sim 200 \text{ m s}^{-1}$) are all different, presumably resulting in the different mean time of the short interarrival time mode. The PIP shows very little contamination by shattered particles. Similarly, the HVPS during the TRMM flight (Fig. 5) shows little contamination, whereas there is a distinct short interarrival time mode at $9 \times 10^{-5} \text{ s}$ that is similar to the value seen for this configuration of aircraft and probe for the CRYSTAL-FACE flight. Finally, the FIRE data (Fig. 6) show very little bimodality in the interarrival time data from either the 2D-C or 2D-P probes.

Figure 7 shows example imagery of particles that have interarrival times shorter than $2 \times 10^{-4} \text{ s}$ (gray images) from the TRMM data and are therefore found in the short interarrival time mode. These particles do not appear to be a product of instrumental noise and would be accepted as valid particles if they passed the other criteria described in section 3.

To provide a more quantitative analysis of the interarrival time data the same method as given in Field et al. (2003) was followed. In the ensuing analysis we have made the implicit assumption that particles are distributed randomly in space. Field et al. showed that a function representing two Poisson processes provided a good fit to the observed distributions of interarrival times obtained from a fast FSSP in ice cloud as follows:

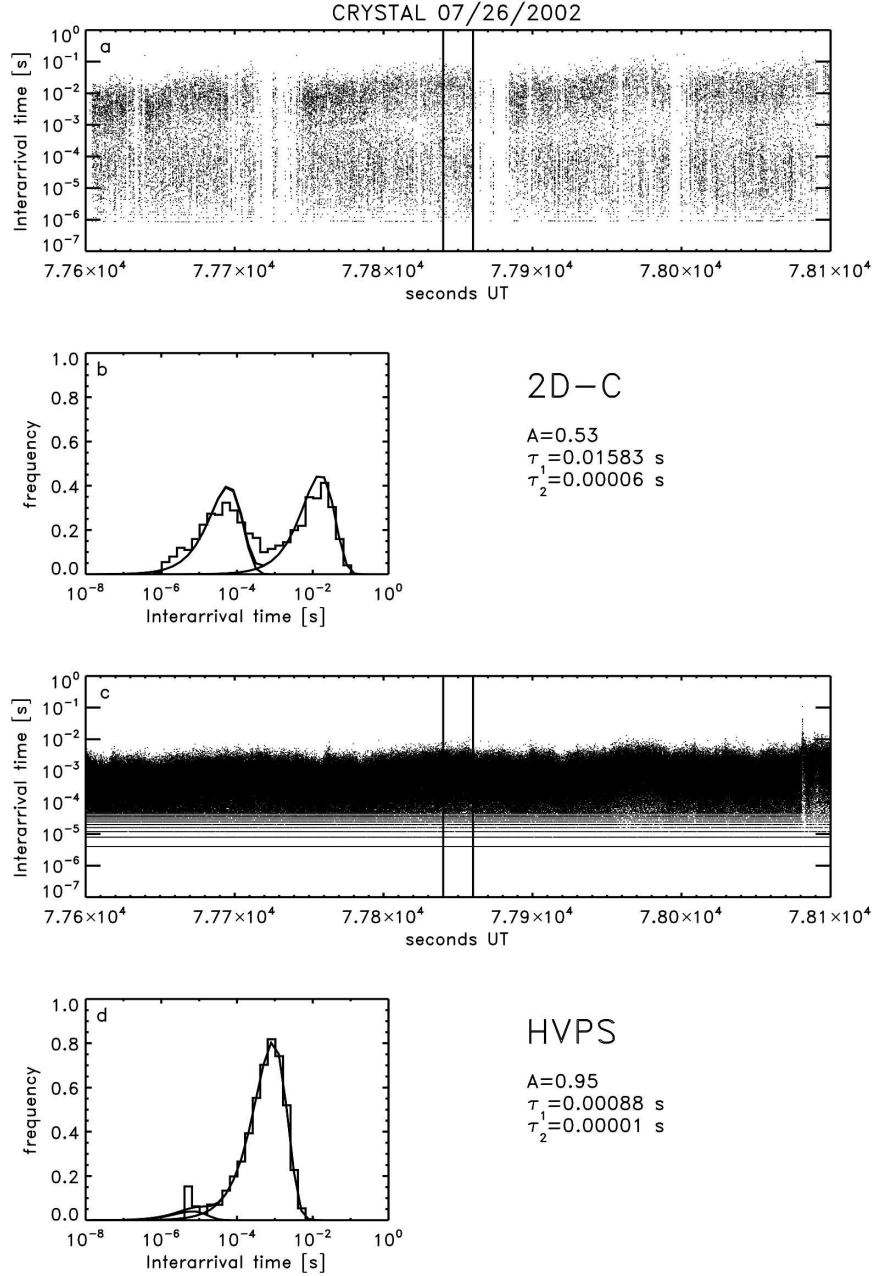


FIG. 3. Interarrival time data for the CRYSTAL-FACE flight (26 Jul 2002). (a) Interarrival times of 500 s from the 2D-C probe. Each point represents the interarrival time of a particle. (b) The stepped line is a histogram (binned logarithmically) of the 20 s of interarrival times bracketed by the vertical lines in (a). The solid lines represent the best-fit function whose parameters are given to the right of the plot. (c) Interarrival times of 500 s from the HVPS probe. Each point represents the interarrival time of a particle. (d) The stepped line is a histogram (binned logarithmically) of the 20 s of interarrival times bracketed by the vertical lines in (c). The solid lines represent the best-fit function whose parameters are given to the right of the plot.

$$P(\Delta t > \Delta t_i) = A \exp\left(-\frac{\Delta t}{\tau_1}\right) + (1 - A) \exp\left(-\frac{\Delta t}{\tau_2}\right),$$

(1)

where $P(\Delta t > \Delta t_i)$ is the probability of finding interarrival times Δt between Δt_i and ∞ . This function is fitted to the observed distribution of interarrival times in semilog space using the nonlinear least squares Leven-

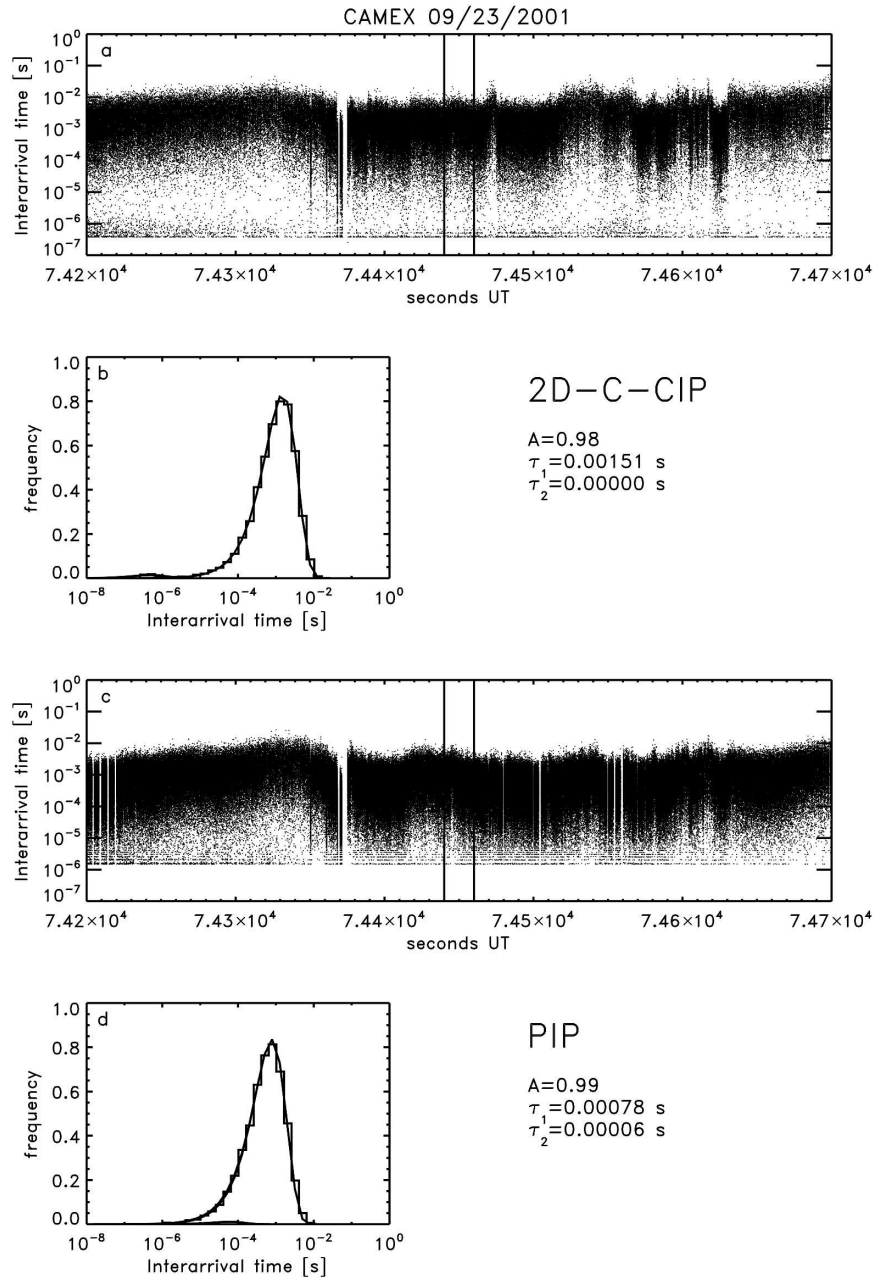


FIG. 4. Interarrival time data for the CAMEX flight (23 Sep 2001). (a) Interarrival times of 500 s from the 2D-C-CIP probe. Each point represents the interarrival time of a particle. (b) The stepped line is a histogram (binned logarithmically) of the 20 s of interarrival times bracketed by the vertical lines in (a). The solid lines represent the best-fit function whose parameters are given to the right of the plot. (c) Interarrival times of 500 s from the PIP probe. Each point represents the interarrival time of a particle. (d) The stepped line is a histogram (binned logarithmically) of the 20 s of interarrival times bracketed by the vertical lines in (c). The solid lines represent the best-fit function whose parameters are given to the right of the plot.

berg-Marquardt method implemented in the Interface Definition Language (IDL) programming language (Research Systems, Inc.) and described in Press (1992) with the following relation:

$$\frac{dP(\Delta t)}{d \ln t} = A \frac{\Delta t}{\tau_1} \exp\left(-\frac{\Delta t}{\tau_1}\right) + (1 - A) \frac{\Delta t}{\tau_2} \exp\left(-\frac{\Delta t}{\tau_2}\right). \quad (2)$$

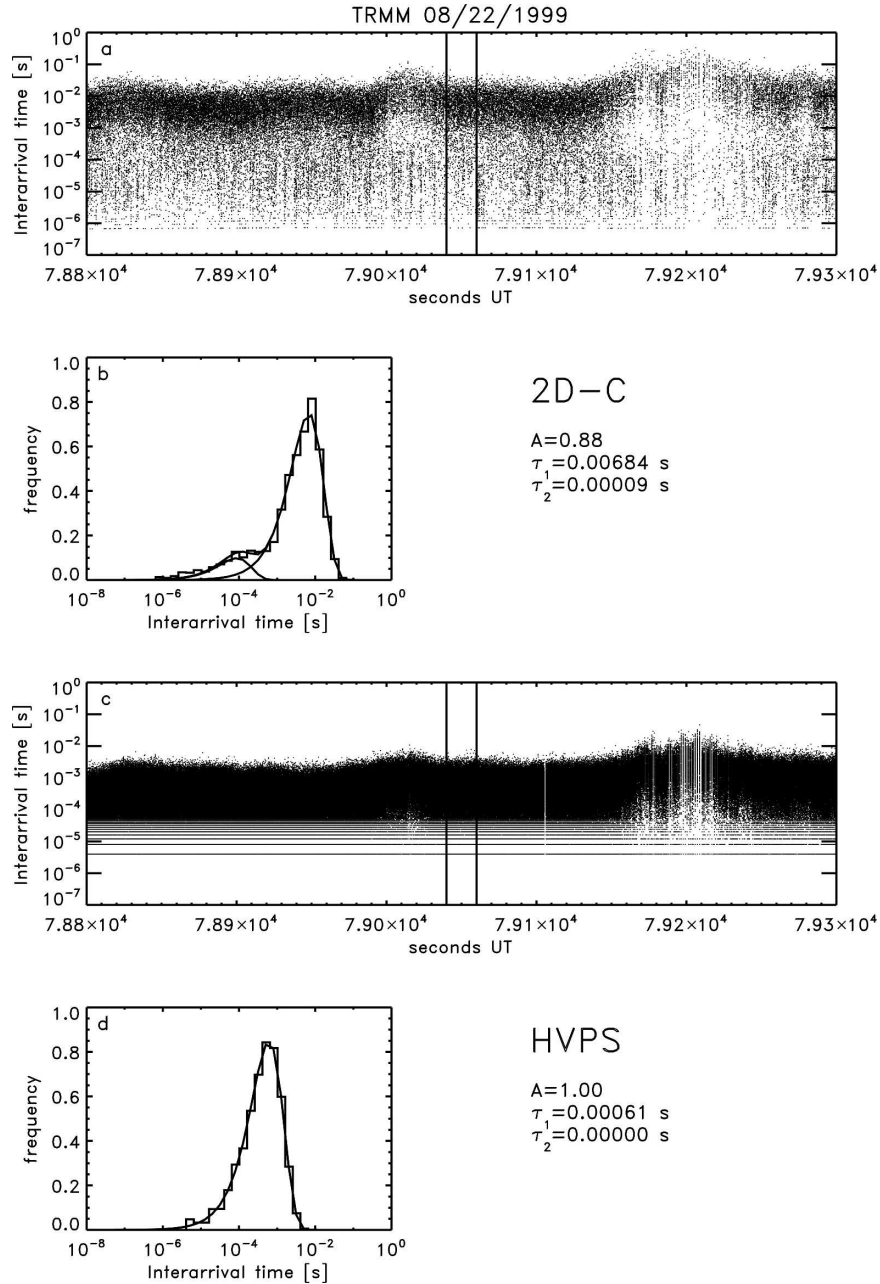


FIG. 5. Interarrival time data for the TRMM flight (22 Aug 1999). (a) Interarrival times of 500 s from the 2D-C probe. Each point represents the interarrival time of a particle. (b) The stepped line is a histogram (binned logarithmically) of the 20 s of interarrival times bracketed by the vertical lines in (a). The solid lines represent the best-fit function whose parameters are given to the right of the plot. (c) Interarrival times of 500 s from the HVPS probe. Each point represents the interarrival time of a particle. (d) The stepped line is a histogram (binned logarithmically) of the 20 s of interarrival times bracketed by the vertical lines in (c). The solid lines represent the best-fit function whose parameters are given to the right of the plot.

The A parameter indicates what fraction of particles are part of the Poisson distribution associated with the mean interarrival time τ_1 , while $(1 - A)$ is the fraction of particles associated with the mean interarrival time

τ_2 . Figures 3b,d, 4b,d, 5b,d, and 6b,d show the result of this fitting for the 20-s period highlighted with the parameters A , τ_1 , and τ_2 given to the right of the histogram. These parameters were obtained over 5-s periods

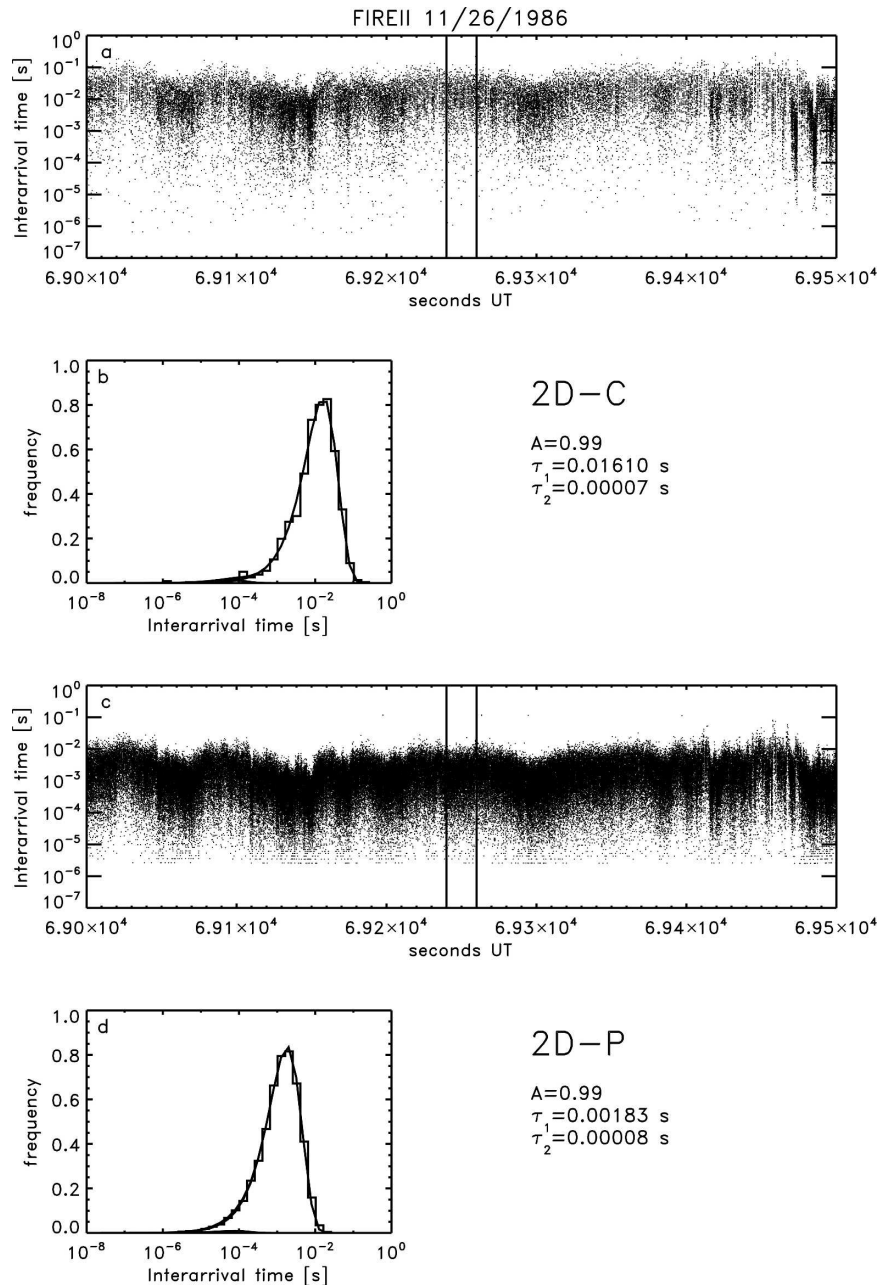


FIG. 6. Interarrival time data for the FIRE flight (26 Nov 1986). (a) Interarrival times of 500 s from the 2D-C probe. Each point represents the interarrival time of a particle. (b) The stepped line is a histogram (binned logarithmically) of the 20 s of interarrival times bracketed by the vertical lines in (a). The solid lines represent the best-fit function whose parameters are given to the right of the plot. (c) Interarrival times of 500 s from the 2D-P probe. Each point represents the interarrival time of a particle. (d) The stepped line is a histogram (binned logarithmically) of the 20 s of interarrival times bracketed by the vertical lines in (c). The solid lines represent the best-fit function whose parameters are given to the right of the plot.

for the entirety of the four flights considered. In Fig. 8, the $(1 - A)$ parameter has been plotted against the OAP-derived mean particle size (ratio of the third and second moments of the particle size distribution for

sizes greater than $100 \mu\text{m}$, i.e., the mass-weighted mean diameter if particle mass is proportional to size squared, and hence bulk density is inversely proportional to particle size) for the 2D-C and 2D-C-CIP, and

TABLE 2. Approximate particle concentrations for OAP probes for a true airspeed of 100 m s^{-1} .

Interarrival time (s)	Interparticle distance (m)	Concentration (cm^{-3})			
		2D-C-CIP	2D-P	HVPS	PIP
10^{-2}	1	0.2	6×10^{-4}	10^{-4}	1.6×10^{-4}
10^{-6}	10^{-4}	200	6	1	16

the HVPS and 2D-P. The exponential slope parameter (λ) is also given for reference. As an aside we note that it is difficult to estimate an error or measure of variability in the computed moments and hence characteristic size (and λ) from a single 5-s sample, but if we assume that an adequate estimate of the error in the moment is given by the Poisson-counting error for the size bin containing the moment-weighted mean size (because this is the most significant contributor to this moment), then we can combine the errors for the ratio of moments in quadrature to give an error for the characteristic size (and λ). After completing this exercise for the data presented here we find that fractional errors (one sigma) in the characteristic size L_{32} (or λ) vary from 0.05 for $L_{32} = 1000 \text{ } \mu\text{m}$ ($\lambda = 30 \text{ cm}^{-1}$) to 0.20 for $L_{32} = 4000 \text{ } \mu\text{m}$ ($\lambda = 7.5 \text{ cm}^{-1}$). However, a simple Poisson-counting error argument ignores the effects of natural variability, which could be just as important. Additionally, it should be noted that 5 s represents between 500 and 1000 m of along-track distance for the aircraft speeds considered here and may exceed the scale of some physical processes. There is a correlation between the mean particle size and the fraction of particles associated with short interarrival times recorded by the 2D-C and 2D-C-CIP probes (Fig. 8a), but there is no obvious correlation for the HVPS and 2D-P probes. For the 2D-C and 2D-C-CIP probes, the fraction of particles associated with the short interarrival time exceeds 10% when the characteristic particle size of the PSD exceeds $1000 \text{ } \mu\text{m}$ or the exponential slope parameter λ falls below 30 cm^{-1} .

5. Interpretation and correction

The measured size distribution is the sum of the real in situ size distribution and an anomalous distribution of debris produced by particles that strike the arms of the probe, shatter and fall into the probe sample volume to be recorded. When the real size distribution contains a higher proportion of large particles, these strike the probe arm with greater energy and potentially generate more and larger debris particles. Therefore, as the real size distribution becomes broader the contribution to the measured distribution from the anomalous debris size distribution increases. The implication is that the lower concentrations of larger particles are more efficient at producing debris that can be

measured by the probe than high concentrations of small particles. To determine the real in situ distribution of particles we simply need to identify and remove the anomalous debris distribution.

This train of shatter products results in measured particles having abnormally short interarrival times as previously recognized in Cooper (1977) and Baumgardner and Dye (1983) and reiterated in Field et al. (2003) and Korolev and Isaac (2005). The lack of correlation exhibited by the results for the HVPS and 2D-P (Fig. 8b) is because the lower time resolution, coarser pixel size, and depth-of-field consideration for smaller particles related to these probes tends to naturally filter out the effect of the shattering. Korolev and Isaac (2005) concentrated on these probes in their analysis and looked at imagery of multiple particles within a single image frame and statistics associated with “zero interarrival time” particles. In the processing used here both of these types of artifact have been removed, but a method of correcting for the effects of the shattered particles is still required.

When the fragments of a shattered particle pass through the sample volume of an OAP, the first fragment will have a normal or long interarrival time close to that of the original unbroken particle from which it was created. The subsequent fragments will have abnormally short interarrival times and so are easily identified, but it will be important to remove the leading particle too. The simplest way of eliminating the latter fragments is to reject in software processing all particles with interarrival times shorter than a chosen threshold value τ_c . A correction must then be made for the legitimate particles that have been filtered out by the thresholding. This correction is based on the assumption that the particles are distributed as a result of a Poisson process with a mean interarrival time of τ_1 . Thus, the correction factor can be found as follows. The fraction of legitimate particles with interarrival times below the threshold is $[1 - \exp(-\tau_c/\tau_1)]$, and because two particles are removed for every one legitimate particle found to have a short interarrival time,¹ the number of particles removed, N_{removed} , will be

¹ Legitimate particles with interarrival times shorter than the threshold tend to occur singly.

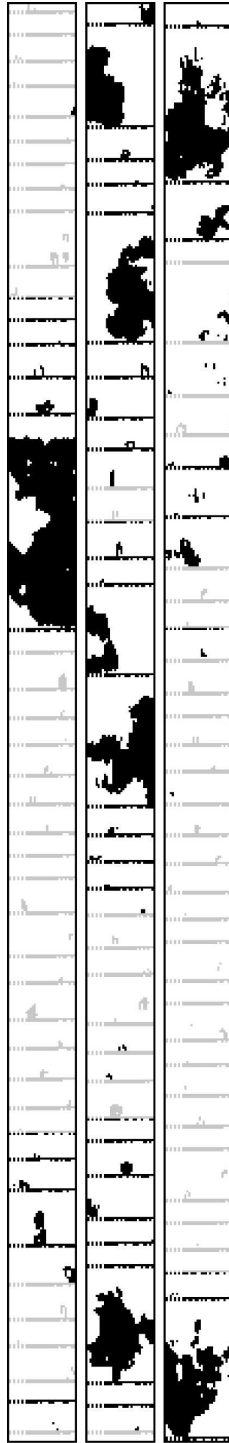


FIG. 7. 2D-C particle buffers from the 22 Aug 1999 TRMM flight. The width of each strip is $800 \mu\text{m}$. The gray particles have an interarrival time shorter than 2×10^{-4} s. Some particles in this image will be rejected for other reasons, but that has not been highlighted for simplicity.

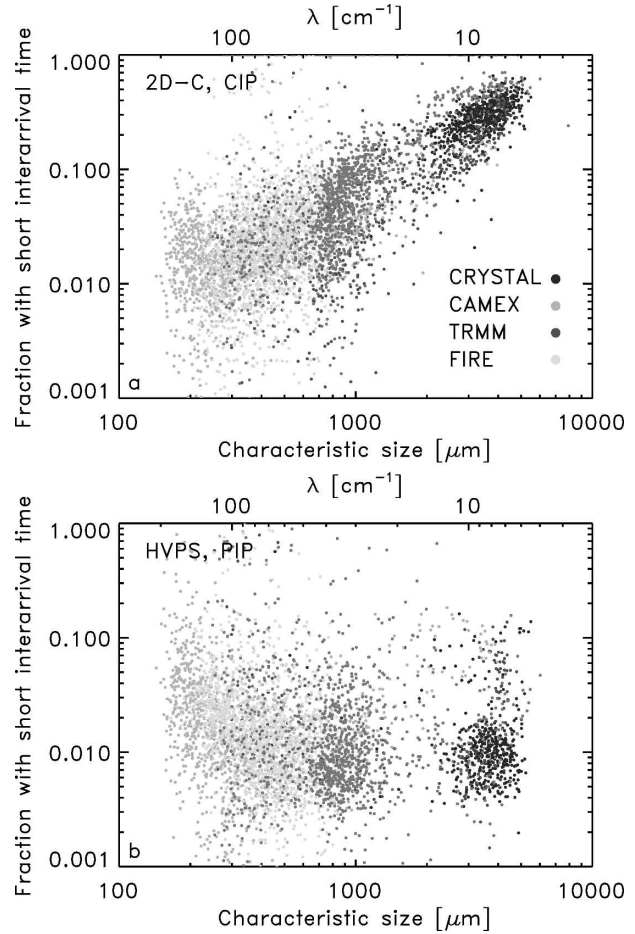


FIG. 8. Fraction of particles in short interarrival time mode ($1 - A$) [see Eq. (1)] vs the characteristic size (ratio of third to second moment of the size distribution for sizes greater than $100 \mu\text{m}$) for 5-s periods throughout the flights. The exponential slope parameter is also given for reference. (a) 2D-C and 2D-C-CIP, and (b) HVPS, PIP, and 2D-P.

$$N_{\text{removed}} = N_{\text{total}} \times 2[1 - \exp(-\tau_c/\tau_1)], \quad (3)$$

where N_{total} is the total number concentration of legitimate particles. The accepted number concentration of legitimate particles is then simply $N_{\text{accepted}} = N_{\text{total}} - N_{\text{removed}}$, or

$$N_{\text{accepted}} = N_{\text{total}} \times [2 \exp(-\tau_c/\tau_1) - 1]. \quad (4)$$

Therefore, the total number concentration of legitimate particles is

$$N_{\text{total}} = N_{\text{accepted}} \times 1/[2 \exp(-\tau_c/\tau_1) - 1]. \quad (5)$$

The results from the previous section suggest that the size distributions measured by the 2D-C probe are most affected by particle shattering and that the processing described in section 3 is sufficient to capture most of the artifacts present on the large precipitation probes.

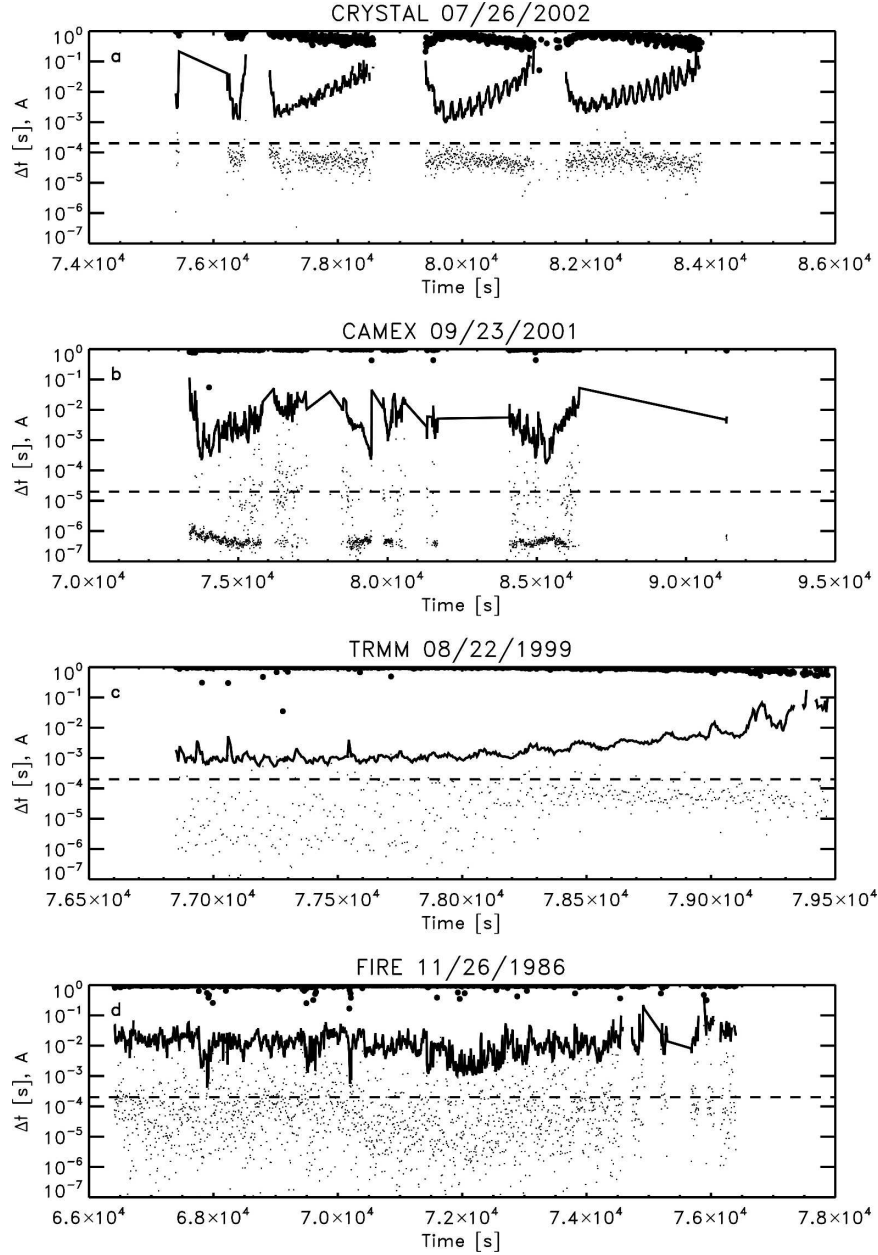


FIG. 9. Plot of fitted parameters as a function of time from the four flights: fraction of particles in long interarrival time mode A (circles), mean time of long interarrival time mode τ_1 (solid line), mean time of short interarrival time mode τ_2 (points), and threshold interarrival time used in each case (dashed line).

Therefore, we attempt to correct the cloud probe size distributions only. To apply this correction we proceed with the following method.

- (i) Carry out “standard” processing of OAP imagery similar to that described in section 3.
- (ii) Eliminate, through software processing, all of the particles with interarrival times less than τ_c . Do not
- eliminate particle interarrival time from integrated probe-elapsed time.
- (iii) Also eliminate the invalid first particle in a train of fragments by removing the particle that precedes particles removed for having a short interarrival time. Do not eliminate particle interarrival time from integrated probe-elapsed time.
- (iv) Multiply the particle concentrations within all size

bins by the correction factor [from Eq. (5)]: $1/[2 \exp(-\tau_c/\tau_1) - 1]$.

The reader may be thinking that the correction factor should simply be $1/\exp(-\tau_c/\tau_1)$, as expected for a Poisson process, but it should be noted that using this correction factor rather than the one in step iv would only account for the legitimate particles eliminated below the interarrival time threshold by step ii, and will not make up for the particles above the threshold that were eliminated for being at the head of the train of fragments by step iii.

The next point to address is the choice of interarrival time threshold. Cooper (1977) utilized an interparticle spacing threshold of 2.5 cm that is equivalent to 2.5×10^{-4} s for an airspeed of 100 m s^{-1} ; Gordon and Marwitz (1986) attempted to filter out particles that had short interarrival times by removing particles with interarrival times (or interparticle spacing) smaller than the mean value. Such a threshold could be considered too harsh. Figure 9 shows the fitted parameters A , τ_1 , and τ_2 as a function of time for the four flights. The first point to note is that the τ_2 , the mean interarrival time associated with the short interarrival time mode, can vary from flight to flight. This is most likely the result of the different aircraft-mounting positions, flight speeds, and breakup modes experienced by ice particles of varying habits encountered. The threshold interarrival time needs to be chosen so that a large fraction of the particles associated with the long interarrival time mode are passed, while still filtering out most of the short interarrival time mode. A threshold set at twice the value of τ_2 will eliminate nearly 90% of the particles associated with the short interarrival time mode. For the CRYSTAL-FACE, TRMM, and FIRE flights a threshold of 2×10^{-4} s was used [essentially the same as the threshold suggested by Cooper (1977)], while for the CAMEX flight a threshold of 1×10^{-5} s was applied. These threshold values represent 800 and 80 time slices for these probes (2D-C and 2D-C-CIP). This suggests that users need to assess the severity of the shattering effects and choice of threshold for the combination of aircraft and probes that are being used.

One example of the correction to the size distribution (5-s average) following steps i–iv, described above, is shown in Fig. 10 for each flight. The correction factors from step iv applied to the distributions shown in Fig. 10 were 1.65, 1.11, 1.00, and 1.01 for the TRMM, CRYSTAL-FACE, CAMEX, and FIRE flights, respectively. This plot shows the size distributions that result from standard processing (dashed) and after using the processing described above to eliminate the effect of shattering (solid). This correction only affects the cloud

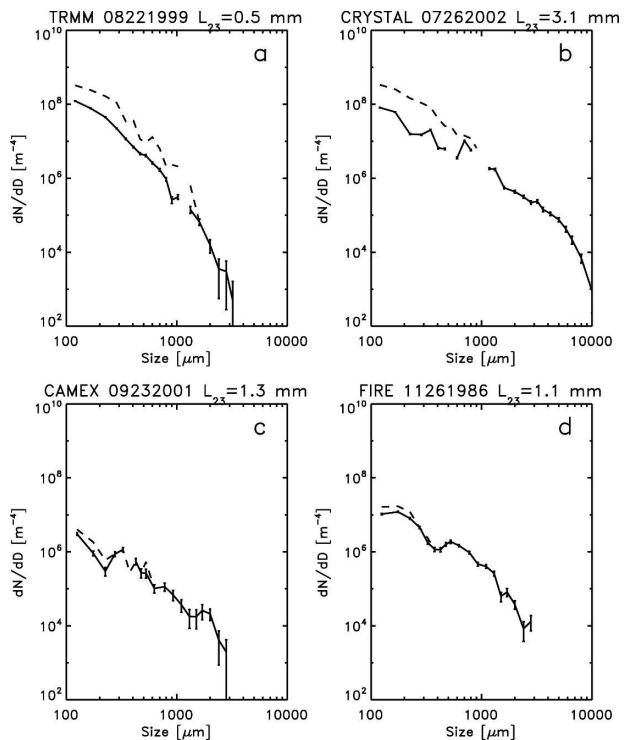


FIG. 10. Examples from the four flights showing the corrected (solid) and uncorrected (dashed) size distributions (5-s average). The characteristic size of the size distribution is also given. Vertical bars represent the Poisson counting error.

probe size ranges, but the precipitation probe part of the distribution has been included to provide context. The range in size of the shatter fragments implied through comparing the uncorrected and corrected size distributions can equally result from physically large fragments entering the sample volume with speeds close to the airspeed or the sampling of smaller fragments with speeds slower than the airspeed. While it cannot be claimed that these examples are representative of all of the size distributions used in this analysis, it can be seen that the point where the size distribution intercepts the y axis is reduced by a factor of 2 or 3 and may have implications for exponential slope fitting to size distributions.

Figure 11 shows the results of eliminating the shattered particles from the size distributions. Plotted are the ratios of moments (particle sizes $>100 \mu\text{m}$) obtained from 5-s-averaged size distributions for the situation in which only the processing described in section 3 was carried out compared to processing suggested in this section. It can be seen that the particle concentration (zeroth moment) is most affected when the size distribution is broad (up to a factor of 4 for characteristic sizes $>3 \text{ mm}$, see Fig. 10a), whereas the second moment that is roughly proportional to ice water con-

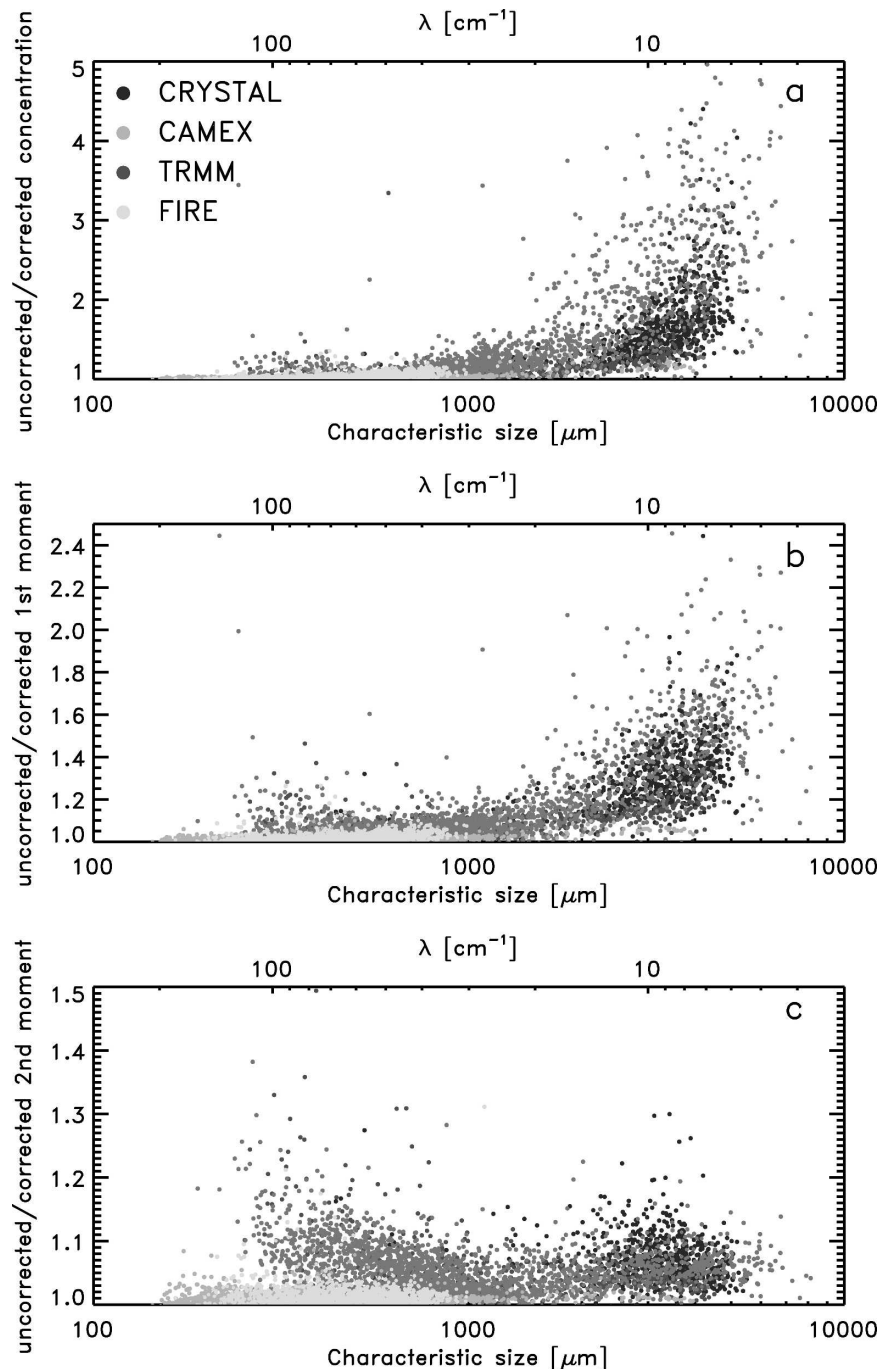


FIG. 11. Plots of the ratios of moments obtained from the uncorrected and corrected size distributions over 5-s periods for particle sizes larger than $100 \mu\text{m}$ vs the characteristic size (ratio of third to second moment of the size distribution): (a) concentration, (b) first moment, and (c) second moment that is approximately proportional to the ice water content.

tent shows most change when the size distribution is narrow (up to 20%–30% for characteristic sizes $<1 \text{ mm}$, see Fig. 10c). This result for the second moment is because when the size distribution is broad [characteristic sizes $>3 \text{ mm}$ or $\lambda < 10 \text{ (cm}^{-1}\text{)}]$ the mass is con-

tained in the large particle size distribution. The large particle distribution is unaffected by the shattering because the shatter fragments are either too small or have too-short interarrival time for the size distribution measured by the precipitation probes to be affected by

them. Even though the effects of shattering are reduced for narrow-sized distributions, they are still sufficient to affect the estimate of the second moment. This result suggests that users need to be aware of the effects of shattering even in cirrus where large particles are absent.

6. Summary

It has been known since the introduction of the optical array probes for studying cloud structure that some filtering is required to remove artifacts produced by collision between ice crystals and probe housings. Shattering of particles during collision with the probe can produce a train of particles that when passing through the sample volume leads to the detection of particles with abnormally short interarrival times. We have demonstrated that the 2D cloud probes are most affected by this artifact and that the numbers of shattered particles detected increases as the size distribution broadens. To remedy the situation, we have made use of a threshold interarrival time (2×10^{-4} s for the 2D-C mounted on the Cessna Citation and King Air and 1×10^{-5} s for the 2D-C-CIP mounted on the DC-8) to filter out particles associated with particle shattering based on inspection of the particle interarrival time data.

Comparison of the uncorrected and corrected size distributions show that concentrations of particles with sizes of up to several hundred microns can be affected by the shattering process. We have not considered the effect on the size distribution for sizes smaller than 100 μm because of the many problems associated with measuring particles smaller than this with these probes (Baumgardner and Korolev 1997; Strapp et al. 2001). Comparison of the moments obtained from the uncorrected and corrected particle size distributions showed that the measured concentrations could be affected by up to a factor of 4 where the mass-weighted mean size was in excess of 3 μm , while the estimate of ice water content was most affected for narrow size distributions and could be overestimated by 20%–30%. In extreme cases the errors could be larger. Consequently, fitted parameters obtained from exponential fitting, for example, will also be in error.

In light of these findings, especially with the advent of new aircraft platforms and cloud probes, it is recommended that OAP users routinely examine plots of particle interarrival times to visually assess whether there is a potential contamination problem for their aircraft/probe configuration and, if required, eliminate the contamination using a method similar to that described here.

As remarked here and in Korolev and Isaac (2005), the rejection of particles based on interarrival time is not entirely satisfactory, especially in situations where particle concentrations are high, such as mixed-phase conditions, where interarrival time thresholding will not be possible because it will adversely affect the sampling of droplets. Also, the correction methodology is based upon the assumption that the particles are randomly distributed, which, although satisfactory as a first approximation, may not be entirely appropriate. New probe designs, adaptations of existing probes, or operation of these probes at lower airspeeds are required to minimize the effects of particle shattering. In particular, the time may now be ripe to revisit the use of holographic techniques (e.g., Fugal et al. 2004). In the past the use of holography has required intensive manual effort. Modern computer technology has reduced this burden and provides a way for the user to sample volumes that are unaffected by particle shattering away from the probe structure.

Acknowledgments. We acknowledge the hard work and dedication of the aircrews and support personnel of the NCAR King Air, University of North Dakota Citation, and NASA DC-8 aircraft that obtained the data used in this paper. We are also grateful to the comments and suggestions provided in reviews from Walter Strapp, Alexei Korolev, and a third anonymous reviewer that helped improve this paper.

REFERENCES

- Baumgardner, D., and J. E. Dye, 1983: The 1982 cloud particle measurement symposium 4–7 May 1982, Boulder, Colo. *Bull. Amer. Meteor. Soc.*, **64**, 366–370.
- , and A. Korolev, 1997: Airspeed corrections for optical array probe sample volumes. *J. Atmos. Oceanic Technol.*, **14**, 1224–1229.
- Cooper, W. A., 1977: Cloud physics investigation by the University of Wyoming in HIPLEX 1977. Bureau of Reclamation Rep. AS 119, 321 pp.
- Field, P. R., R. Wood, P. R. A. Brown, P. H. Kaye, E. Hirst, R. Greenaway, and J. A. Smith, 2003: Ice particle interarrival times measured with a fast FSSP. *J. Atmos. Oceanic Technol.*, **20**, 249–261.
- Fugal, J. P., R. A. Shaw, E. W. Saw, and A. V. Sergeev, 2004: Airborne digital holographic system for cloud particle measurements. *Appl. Opt.*, **43**, 5987–5995.
- Gardiner, B. A., and J. Hallett, 1985: Degradation of in-cloud forward scattering spectrometer probe measurements in the presence of ice particles. *J. Atmos. Oceanic Technol.*, **2**, 171–180.
- Gayet, J.-F., G. Febvre, and H. Larsen, 1996: The reliability of the PMS FSSP in the presence of small ice crystals. *J. Atmos. Oceanic Technol.*, **13**, 1300–1310.
- Gordon, G. L., and J. D. Marwitz, 1986: Hydrometeor evolution

- in rainbands over the California valley. *J. Atmos. Sci.*, **43**, 1087–1100.
- Hallett, J., 1976: Measurement of size, concentration and structure of atmospheric particulates by the airborne continuous particle replicator. Air Force Geophysics Laboratory, Air Force Systems Command, United States Air Force, Hanscom AFB, Tech. Rep. AFGL-TR-76-0419, 92 pp.
- Heymsfield, A. J., and J. L. Parrish, 1978: Computation technique for increasing effective sampling volume of pms1 2-dimensional particle-size spectrometer. *J. Appl. Meteor.*, **17**, 1566–1572.
- , and D. Baumgardner, 1985: Summary of a workshop on processing 2D probe data. *Bull. Amer. Meteor. Soc.*, **66**, 437–440.
- Jensen, J. B., and H. Granek, 2002: Optoelectronic simulation of the PMS 260X optical array probe and application to drizzle in stratocumulus. *J. Atmos. Oceanic Technol.*, **19**, 568–585.
- Knollenberg, R. G., 1970: The optical array: An alternative to extinction and scattering for particle size measurements. *J. Appl. Meteor.*, **9**, 86–103.
- , 1981: Techniques for probing cloud microstructure. *Clouds: Their Formation, Optical Properties and Effects*, P. V. Hobbs and A. Deepak, Eds., Academic Press, 15–91.
- Korolev, A. V., and G. A. Isaac, 2005: Shattering during sampling by OAPs and HVPS. Part 1: Snow particles. *J. Atmos. Oceanic Technol.*, **22**, 528–542.
- Press, W. H., 1992: *Numerical Recipes in C: The Art of Scientific Computing*. Cambridge University Press, 994 pp.
- Strapp, J. W., F. Albers, A. Reuter, A. V. Korolev, U. Maixner, E. Rashke, and Z. Vukovic, 2001: Laboratory measurements of the response of a PMS OAP-2DC. *J. Atmos. Oceanic Technol.*, **18**, 1150–1170.